AGU ADVANCING EARTH AND SPACE SCIENCES

JGR Earth Surface

RESEARCH ARTICLE
10.1029/2025JF008367

Post-Collapse Ice Cliff Backwasting at the Marmolada Glacier Observed by Terrestrial Radar Interferometry

Alessio Gusmeroli[1], Tommaso Carlà[2], Davide Leva[1], Carlo Rivolta[1], Fabio Villa[1], and Nicola Casagli[2]

[1]Ellegi srl, Milan, Italy, [2]Department of Earth Sciences, University of Florence, Florence, Italy

Key Points:

- Radar monitoring of the Marmolada Glacier's ice cliff after its 2022 collapse showed no further downslope instability
- Temperature-driven backwasting was observed on the ice cliff, with faster retreat on the sun-exposed rim than the shaded wall
- Ice melt on slowly moving glacier cliffs can be observed in near real-time with terrestrial radar interferometry

Correspondence to:

T. Carlà,
tommaso.carla@unifi.it

Citation:

Gusmeroli, A., Carlà, T., Leva, D., Rivolta, C., Villa, F., & Casagli, N. (2026). Post-collapse ice cliff backwasting at the Marmolada Glacier observed by terrestrial radar interferometry. *Journal of Geophysical Research: Earth Surface*, *131*, e2025JF008367. https://doi.org/10.1029/2025JF008367

Received 10 MAR 2025
Accepted 20 FEB 2026

Abstract

The unexpected collapse of the Marmolada Glacier in the Italian Alps on 3 July 2022, caused 11 fatalities and emphasized the need for a deeper understanding of unstable glaciers. In response, we initiated a radar monitoring campaign to assess the stability of the remaining ice cliff and obtained a near-continuous data set of displacement at sub-hourly resolution and sub-millimeter accuracy. The survey spanned July 4–October 2, covering most of the ablation season and allowing insights into the post-collapse evolution of the potentially unstable scar. Rather than observing downslope motion, our measurements revealed progressive ice cliff backwasting driven by melt, with overall displacements up to 1.2 m on the sun-exposed rim and about three times smaller on the shaded wall. The observed pattern suggests that the wall retreated more slowly than the rim, consistent with typical radiation-driven ice cliff morphologies. Daily backwasting peaked at 53 ± 1 mm d^{-1} on the hottest day and fluctuated with air temperature. Sub-freezing temperatures halted the melt, revealing minor displacements toward the sensor, consistent with ice flow of up to 6 ± 1 mm d^{-1}. Correlation analyses confirmed a strong link between daily backwasting rates and air temperature (Spearman coefficient $\rho = 0.80$ at the rim). Independent estimates of backwasting from topographic data were consistent with our measurements, demonstrating the potential of terrestrial radar interferometry for studying ice cliff morphodynamics.

Plain Language Summary

After a deadly ice collapse on Marmolada Glacier in the Italian Alps in July 2022, we installed a radar instrument to monitor whether the remaining steep ice cliff would become unstable again. Unlike previous collapses at other glaciers, after the collapse, we did not observe any signs of significant downslope movement or further failure. Instead, the radar detected that the ice cliff steadily retreated away from the instrument over the summer, mainly due to melting driven by warm air temperatures and sunlight. The rate of melting varied across the cliff face, with faster retreat near the upper rim and slower changes in shaded areas. When temperatures fell below freezing, the cliff showed small movements in the opposite direction, likely reflecting slow ice deformation. These results show that radar interferometry can be a valuable tool not only for detecting dangerous collapses but also for measuring how ice cliffs waste away over time.

1. Introduction

The sudden collapse of a section of the Marmolada Glacier in the Italian Alps on 3 July 2022 resulted in 11 fatalities and brought widespread attention to the growing risks posed by unstable ice masses in a warming mountain cryosphere (Bondesan & Francese, 2023; Francese et al., 2024). Ice avalanches are gravity-driven break-offs originating from steep glaciers (Alean, 1985; Röthlisberger, 1977). These events range from minor detachments to large-scale collapses involving millions of cubic meters of ice (Jacquemart et al., 2024), and even relatively small failures can be devastating, particularly in the European Alps where many people access the mountains for recreation. Despite their relevance, ice avalanche dynamics remain poorly constrained due to the infrequency of such events and the logistical challenges of collecting field observations in remote, high-altitude environments.

The mechanisms driving glacier break-off are complex, involving an interplay between thermal and structural factors. Key controls include the thermal regime at the ice bedrock interface (e.g., warm, wet-based vs. cold, dry-based conditions) and the geometry of both the glacier and its underlying substrate (Faillettaz et al., 2015; Jacquemart et al., 2024). One common consequence of glacier break-off is the formation of newly exposed, sub-vertical ice cliffs at the detachment zone (Alean, 1985; Iken, 1977; Pralong & Funk, 2006). These steep features are often unstable and may initiate recurrent icefalls (Chiarle et al., 2022; Faillettaz et al., 2015; Giordan

Table 1
Post-Collapse Ice Cliff Evolution for Known Ice Avalanches Described in the Literature

Location	Volume (m^3)	Behavior	Reference
Eiger, Switzerland	1.5×10^4	Slow down, recurrent break offs	1, 2
Grandes Jorasses, Italy	1×10^5	Second large collapse 5 days after the first	3
Planpincieux, Italy	$1–5 \times 10^4$	Recurrent icefalls from unstable cliff	4
Weisshorn, Switzerland	$1–5 \times 10^4$	Second large collapse 6 days after the first	5
Marmolada, Italy	7×10^4	Stability, and ice cliff backwasting	6 and this study

Note. (1): Margreth et al. (2017), (2): Chmiel et al. (2023), (3): Faillettaz et al. (2016), (4): Giordan et al. (2020), (5): Faillettaz et al. (2011), (6) Francese et al. (2024).

et al., 2020; Pralong & Funk, 2006), introducing ongoing hazards even after the primary collapse (Table 1 and references therein).

In response to the Marmolada Glacier collapse, we rapidly deployed a terrestrial radar interferometer (TRI) to monitor the stability of the newly exposed ice cliff and to support ongoing search and rescue operations. TRI is routinely used in landslide and rockfall monitoring (Casagli et al., 2023), and provides high-resolution measurements (with repeat intervals of minutes) of glacier surface displacement toward the instrument's line of sight (LOS) (Allstadt et al., 2015; Chmiel et al., 2023; Liu et al., 2019; Margreth et al., 2017; Noferini et al., 2009; Perret et al., 2021; Riesen et al., 2011). Prior to deployment, based on observations from previous collapses, we hypothesized two potential post-event scenarios: (a) the occurrence of recurrent icefalls, triggered by the detachment of unstable ice lamellae, as reported at the Eiger (Margreth et al., 2017) and Planpincieux Glacier (Giordan et al., 2020); and (b) the potential for a second, large collapse occurring a few days after the initial failure, as seen at the Grandes Jorasses (Faillettaz et al., 2016) and Weisshorn (Faillettaz et al., 2011). For both scenarios we were expecting that the TRI would detect acceleration in ice-cliff displacement toward the LOS, providing early indications of renewed instability.

Contrary to our expectations, the Marmolada ice cliff did not exhibit net downslope motion toward the radar sensor. Instead, it migrated slowly away from the sensor over the observation period. In this paper, we report on this unexpected set of observations and explore their implications for understanding post-collapse glacier dynamics. Specifically, we use TRI to investigate the melt-driven backwasting (retreat away from the radar) of the exposed ice cliff and assess the capacity of TRI to detect not only dynamic ice motion, but also surface melt. While TRI is typically employed to measure glacier displacement toward the sensor—resulting in LOS shortening—our data revealed a consistent LOS lengthening throughout the monitoring period. We interpret this signal as spatially variable retreat (backwasting) due to melt, occurring within a slowly moving ice cliff. First, we quantify the spatial variability of surface melt observed along the cliff face. We then assess its temporal evolution and examine the relationship between LOS displacement and air temperature. Finally, we discuss the implications of these findings for understanding both the processes that contributed to the post-collapse evolution of the Marmolada ice cliff, the challenges of TRI glacier monitoring and the broader retreat dynamics of steep glacier fronts.

2. Study Site

This study focuses on the evolution of the remaining ice cliff which formed immediately after the collapse of a small section of the Marmolada Glacier in Northern Italy (Figures 1 and 2). This sub-vertical, north-facing wall was left as a scar on 3 July 2022 when a mass of 64,000 t of water, ice and debris avalanched for about 2 km down the slope (Bondesan & Francese, 2023), killing 11 mountaineers. The ice cliff, at an elevation of 3,213 m, was part of a small, isolated cirque glacier to the east of Punta Rocca (Figure 1) which used to be connected to the main body of the Marmolada Glacier. The Punta Rocca cirque glacier prior to the collapse was a 160 m wide and 140 m long shallow cirque with an average slope of ∼30° (Bondesan & Francese, 2023). The July 3 event drastically changed the shape of the terminus into a sub-vertical frontal ice wall 23 m tall and 70 m long: an optimal target for the radar technique employed in this work (Figure 2).

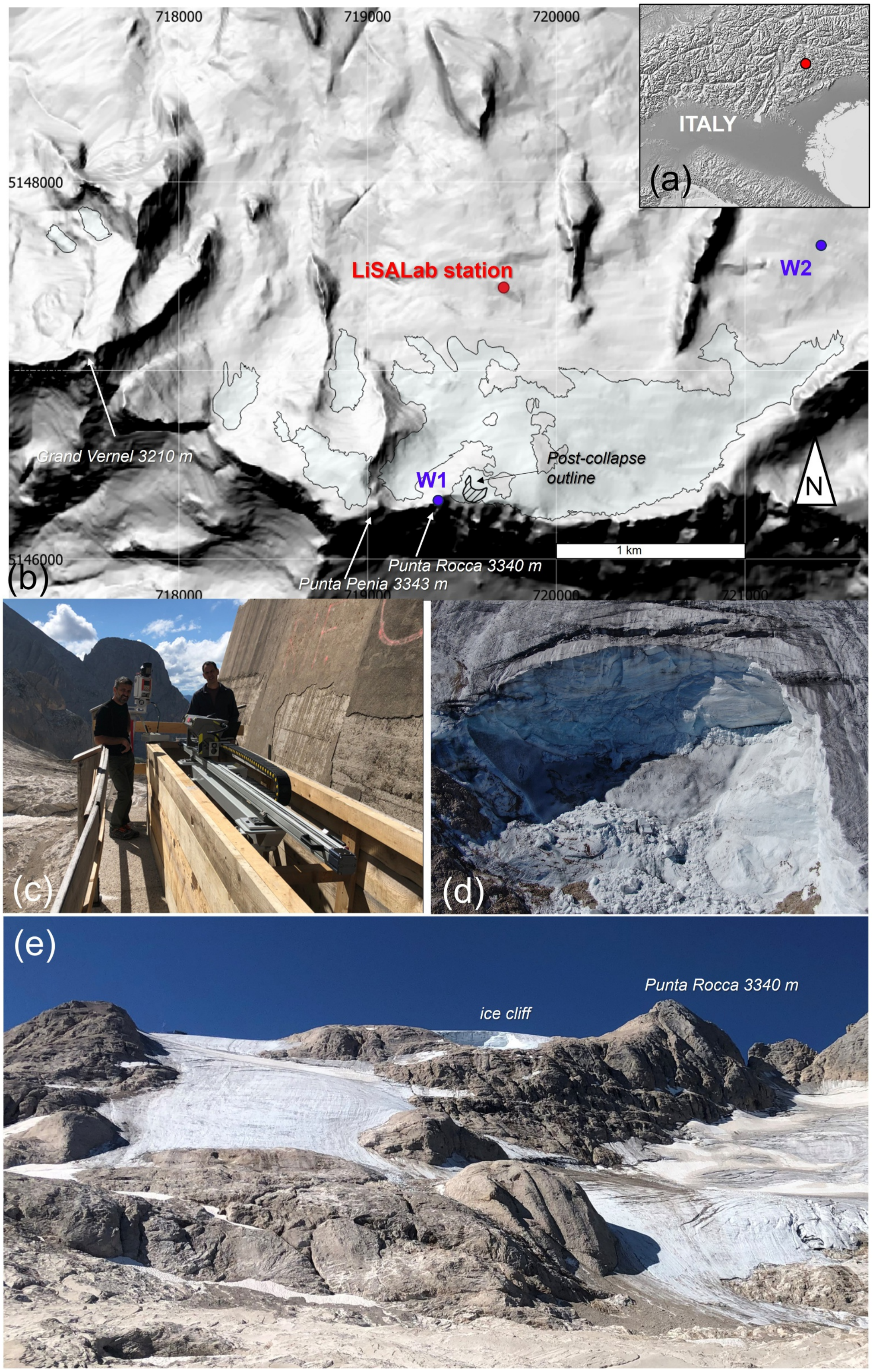

Figure 1. Map overview of the study site (a) and of the Marmolada Group in Northern Italy (b) with indication of the main mountain peaks, the LiSALab© measuring station (red label), the post collapse outline of the Punta Rocca glacier and the two weather stations used in this study (W1 and W2). Glacier outlines from Paul et al. (2019); terrain data from Tarquini et al. (2007). Insets (c)–(e) show the radar instrument, a detailed view of the ice cliff and a view of the Marmolada glacier taken from the radar station.

10.1029/2025JF008367

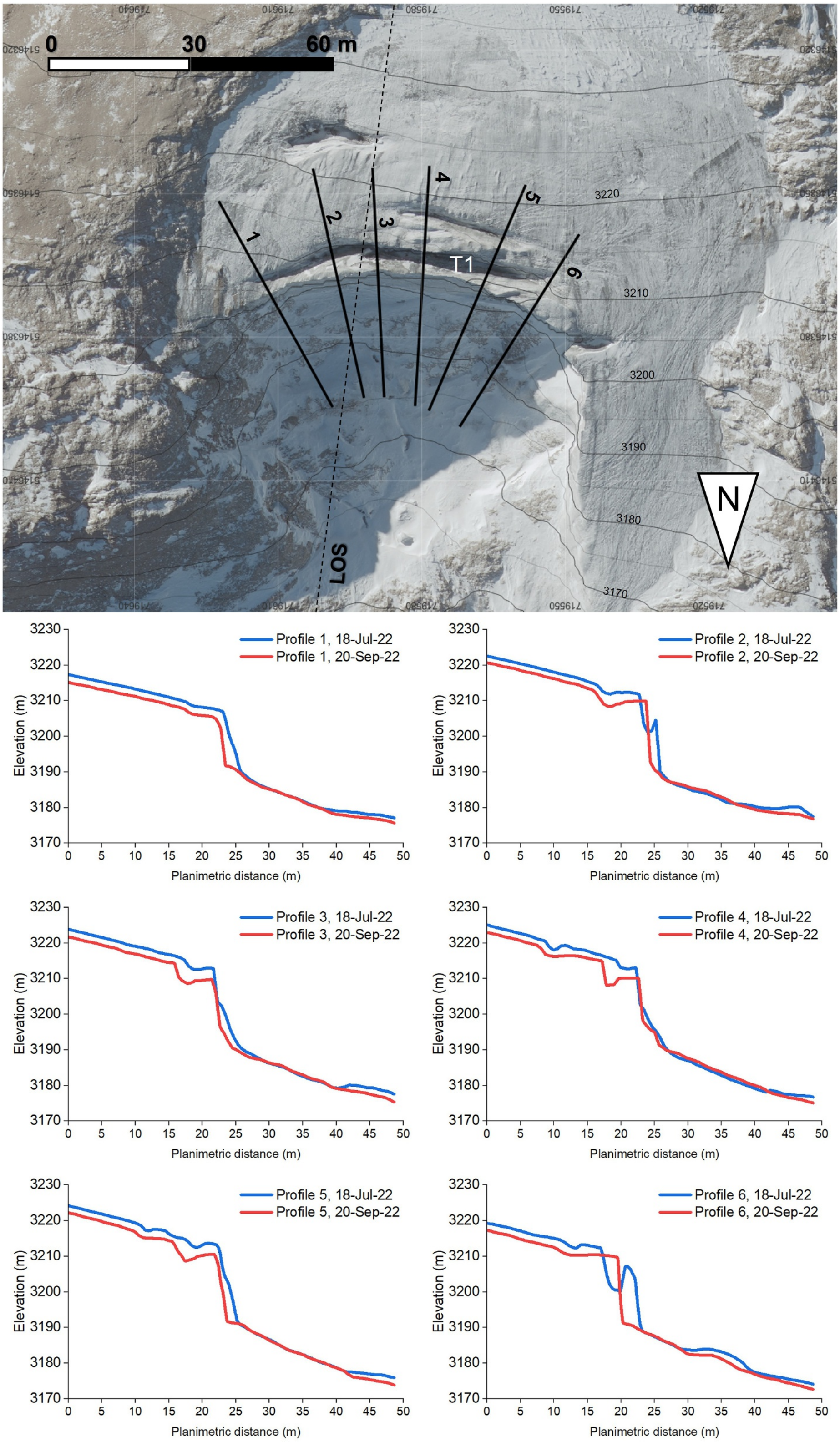

Figure 2. Detailed topography of the Marmolada glacier ice cliff in summer 2022. At the top, digital surface model and aerial photo of the study area in September 2022. Markings show the transverse crevasse T1 and the LOS profile (Figure 3), as well as the traces of six along-cliff cross-sections (shown at the bottom) which highlight the overall retreat of the ice cliff in summer 2022.

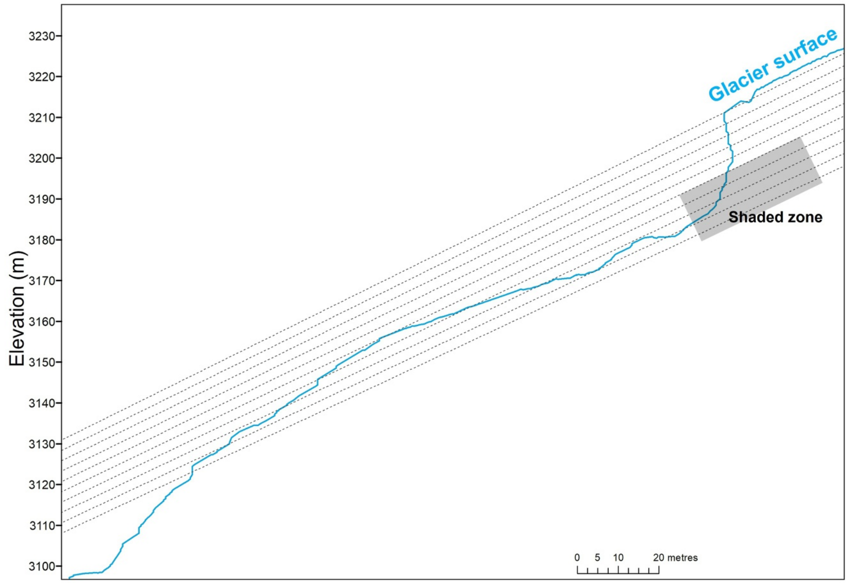

Figure 3. Modeled LOS vectors superimposed to the profile LOS on the Marmolada Glacier ice cliff. Profile position is given in Figure 2. The LOS is parallel to the glacier surface and perpendicular to the ice cliff wall.

3. Methods

3.1. Radar Data Campaign

The day after the collapse, as part of the emergency-response that followed, the Center for Civil Protection of the University of Florence started a monitoring effort to verify the stability of the remaining ice cliff and support search and rescue operations. In this framework, on 4 July 2022 we deployed a LiSALab© TRI system 1.2 km to the north of the ice cliff. The system is based on the LiSA© (Linear Synthetic Aperture) technology developed by the European Commission Joint Research Center (Leva et al., 2003; Tarchi et al., 1999) and has since been used in numerous studies on landslides (Crosta et al., 2014; Lombardi et al., 2017; Tarchi et al., 2003), rock slopes (Carlà et al., 2019, 2024; Kristensen et al., 2021; Rouyet et al., 2017), volcanoes (Di Traglia et al., 2014), glaciers (Perret et al., 2021) and snow avalanches (Skrede et al., 2016). Specifically, it is a stepped frequency radar that illuminates the slope with transmitting and receiving antennas mounted on a moving unit that synthesize a linear aperture along a 3 m long axis (Leva et al., 2003; Tarchi et al., 1999, 2003).

The main outputs of these radar acquisitions are complex images, which provide information on both the radar amplitude and phase. The amplitude is a function of the target's dielectric properties, while the phase depends on the target-to-sensor distance, the dielectric properties of the medium through which the radar signal traveled, and the properties of the reflecting surface. At the radar frequencies used in this study (∼17.2 GHz), signal penetration into bare temperate ice wall is generally considered negligible. Unlike snow, Ku-band radar returns from glacier ice are dominated by surface scattering (Cooper & Smith, 2019; Rott & Mätzler, 1987). Furthermore, TRI relies on frequent, closely spaced acquisitions, minimizing potential biases due to temporal variation in signal penetration depth.

The instrument was installed on top of a steel frame bolted to a concrete basement on the back of the service building of the Rifugio Ghiacciaio Marmolada and sheltered within a wooden skirt capped by a radar-transparent dome (Figures 1c and 1d). The deployment of the full LiSALab© monitoring station relied on transportation by helicopter and, overall, involved a few hours of work including the installation of communication devices to allow remote data analysis and instrument control. The position of the system in respect to the target implied a LOS roughly parallel to the glacier's surface and perpendicular to the ice cliff body (Figure 3). The presence of a rocky hill in the glacier fore-field caused the foot of the ice cliff to be out of the field of view of the radar. Nonetheless, since the wall of the ice cliff was perpendicular to the LOS, the survey configuration was optimal to detect LOS displacement over the ice cliff.

10.1029/2025JF008367

Table 2
Main Characteristics of the LiSALab© System and Measurement Parameters for the Ice Cliff Monitoring

Parameter	Value
Frequency band (GHz)	17.15–17.25
Aperture (m)	3.0
Ice cliff distance (m)	1,200
Ice cliff elevation (m a.s.l.)	3,213
Sensor elevation (m a.s.l.)	2678
Spatial resolution at 1,200 m (range—m)	1.5
Spatial resolution at 1,200 m (azimuth—m)	3.5

Radar data acquisition began on the evening of 4 July 2022, and continued nearly continuously throughout the summer, with an acquisition rate of one radar image approximately every 90 s (roughly 1,000 images per day). Due to the remote location, the primary power supply relied on a combination of solar panels and a manually triggered diesel generator located at the nearby Rifugio Ghiacciaio Marmolada. This power system, designed to meet the basic electricity demands of the mountain hut, experienced various power outages which caused acquisition breaks on 35 of the 91 days of monitoring.

The initial goal of the campaign was real-time monitoring to assess the stability of the ice cliff and support search-and-rescue operations. Once these operations concluded, the system continued to assist decision-makers in evaluating the glacier's stability and collected data until the fall season. This provided a unique opportunity to gather an almost continuous data set, which captured the evolution of the ice cliff throughout the ablation season. The system was eventually removed on 2 October 2022. Measurement characteristics and parameters used in radar acquisition and processing are summarized in Table 2.

3.2. Radar Data Processing and Uncertainty Analysis

The processing workflow followed typical procedures for differential interferometry and included radar data focusing, atmospheric phase-screen compensation, interferometric stacking and coherence masking (Fortuny & Sieber, 1994; Kristensen et al., 2021; Leva et al., 2003; Pieraccini & Miccinesi, 2019; Tarchi et al., 1999, 2003). The stacking procedure reduced the data set from approximately 1,000 images per day to approximately 49 images per day, corresponding to a displacement map every ~30 min. This 30-min interval was deemed optimal after preliminary analyses of unstacked radar images, as it was long enough to enhance the signal-to-noise ratio, yet short enough to avoid measurement ambiguities caused by phase wrapping (Goldstein et al., 1988).

The resulting set of stacked image pairs was analyzed to obtain three main data sets, which are presented in this paper to show the spatial and temporal variability of measured displacement. These data sets included: (a) a cumulative displacement map derived from the sum of all available pairs, (b) time series of measured cumulative displacement at two locations on the ice cliff, and (c) a selected set of displacement maps chosen for their particular relevance and representativeness, which provided further substantiation and interpretation of the results presented here.

Daily displacement estimates were derived directly by daily cumulative sums. Days with incomplete data were generally discarded from the analysis, however, there were nine almost-complete days (≥75% of daily acquisitions) which we deemed useful observations and were not discarded from the computation. For these days we extrapolated daily displacement from partial sums using a linear factor $N_{\mathrm{MAX}}/N_{\mathrm{DAY}}$ whereas N_{MAX} is the number of cumulated images on a complete day (49) and N_{DAY} is the number of images acquired during that particular day. The magnitude of this extrapolation was typically small (average correction of 0.4 ± 1.5 mm) and allowed us to maintain daily displacement measurements which otherwise we would have discarded.

We evaluated the uncertainties in our measurements by quantifying the mean differential displacement over stable areas in the proglacial zone. This analysis, performed on all available pairs over a sample of outcropping bedrock, yielded a value of 0.1 ± 0.2 mm (average value ± one standard deviation). It thus follows that the total uncertainty for displacement measurements derived from one image pair is ±0.2 mm. For cumulative values, we used the standard rule of error propagation in sums (Topping, 1972). This rule states that the combined uncertainty of two quantities equals the square root of the sum of the squares of the individual uncertainties. By propagating the uncertainty, we obtained a value of ±1.4 mm for daily displacement estimates.

3.3. Topographic Data

Post-collapse topographic data were used to evaluate ice cliff evolution and obtain a comparison with the TRI data. At the time of the emergency-response, unfortunately, there were no plans for the acquisition of high-resolution topographic data which could have been used for detailed joint analyses (e.g., time-lapse terrestrial laser scanning throughout the monitoring period). For this reason the only comparison which we were able to

Table 3
Topographic Data Sets Used in This Study

Date	Source	Type	Spatial resolution
8 July 2022	UAV photogrammetry	PC	0.5 points per m^2
18 July 2022	UAV photogrammetry	PC	0.7 points per m^2
9 September 2022	Airborne lidar	DSM	0.5 m × 0.5 m

Note. PC (Point Cloud), DSM (Digital Surface Model).

make for this study relies on data sets which were not specifically acquired for our study but were kindly provided by the Provincia di Trento.

The topographic data sets used in this study are listed in Table 3: in particular, local authorities acquired two photogrammetric surveys of the ice cliff in July by means of commonly used commercial drones and processing tools for photogrammetric point cloud reconstruction; in September, another survey was then performed by routine wide-area, airborne lidar-based techniques of topographic mapping. While the exact vertical accuracy of the used topographic products is not precisely known (given that they were provided by a third party, as previously mentioned), this is certainly an order of magnitude lower than the spatial resolution achieved by our GBInSAR in the described configuration. In Figure 2 we show the September 2022 digital surface model and a July–September comparison on 6 sections over the ice cliff showing an overall retreat of ∼1–1.5 m of the ice cliff position from 18 July to 20 September 2022.

We quantified overall retreat of the ice cliff between July and September 2022 by measuring, along the ice cliff rim, the point-to-point distance along the LOS direction. The spatial resolution and the coverage of the comparison was limited to the pixel-spacing and the regions covered by the September 2022 data set (0.5 m and coverage on the ice cliff rim). Coverage for the September 2022 data set was not optimal as the digital surface model was focused on the top of the ice cliff and not on the vertical wall; as such the sub vertical wall was only partially sampled and only data on the ice cliff rim were available for comparison (Figure 2).

3.4. Air Temperature Data

Hourly air temperature data were available from two automatic weather stations operated by ARPA Veneto (Punta Rocca, W1 and Sas Da Mul W2—position in Figure 1). Data from Punta Rocca were used for all analyses as the station, operated by ARPA Veneto and located at 3,250 m at the top of the mountain, was ∼250 m from the ice cliff. The Sas Da Mul data, located at lower elevation, were only used as supporting data set in the discussion of our main results.

3.5. Correction of TRI Displacement for Missing Data

In order to compare topographic and TRI data we developed a simple correction that accounts for missing data in the TRI data set. This was necessary because the topographic data comparison refers to the full period between 8 July and 20 September 2022, whereas, during this time period, the TRI data set had 22 missing or incomplete days caused by power outages that need to be accounted for. To bridge this gap and obtain a more meaningful comparison, we estimated total displacement over the period (T_{LOS}) as the sum of the displacement from complete TRI days (P_{LOS}) and a correction factor (Δ_{corr}) to account for the missing days.

The correction was derived using a simple and widely used approach based on the relationship between cumulative melt and the sum of positive degree days (Braithwaite, 1995; Hock, 1999; Ohmura, 2001). We performed a linear regression of positive degree days against observed displacement on the ice wall rim. Where Punta Rocca temperature data were missing, we used Sas Da Mul records, adjusted by the average temperature difference between the two stations. Given the robustness of PDD-melt correlations in glaciology, this assumption is sufficient for our purpose here: a simple inter comparison of displacement magnitudes, not a predictive model.

4. Measurements Results

4.1. Initial Observations: The Ice Cliff Moved Away From the LOS

The first result that immediately emerged during the TRI monitoring was that the ice cliff did not exhibit further instabilities but instead it experienced overall net displacement away from the LOS of the sensor (Figure 4). In the early part of the monitoring there was little displacement (Figures 4a1–4a3, July 7) and, as the monitoring period continued, it became apparent that the displacement away from the LOS of the radar grew during the warmest part of the day (Figures 4b1–4b3). For example, on July 21 the displacement on the ice cliff increased from being negligible at night to ∼2 mm h^{-1} early in the morning and reached the value of ∼3.5 mm h^{-1} in the afternoon. Finally, in some days such as 4 August 2022 the ice cliff experienced somewhat continuous displacement

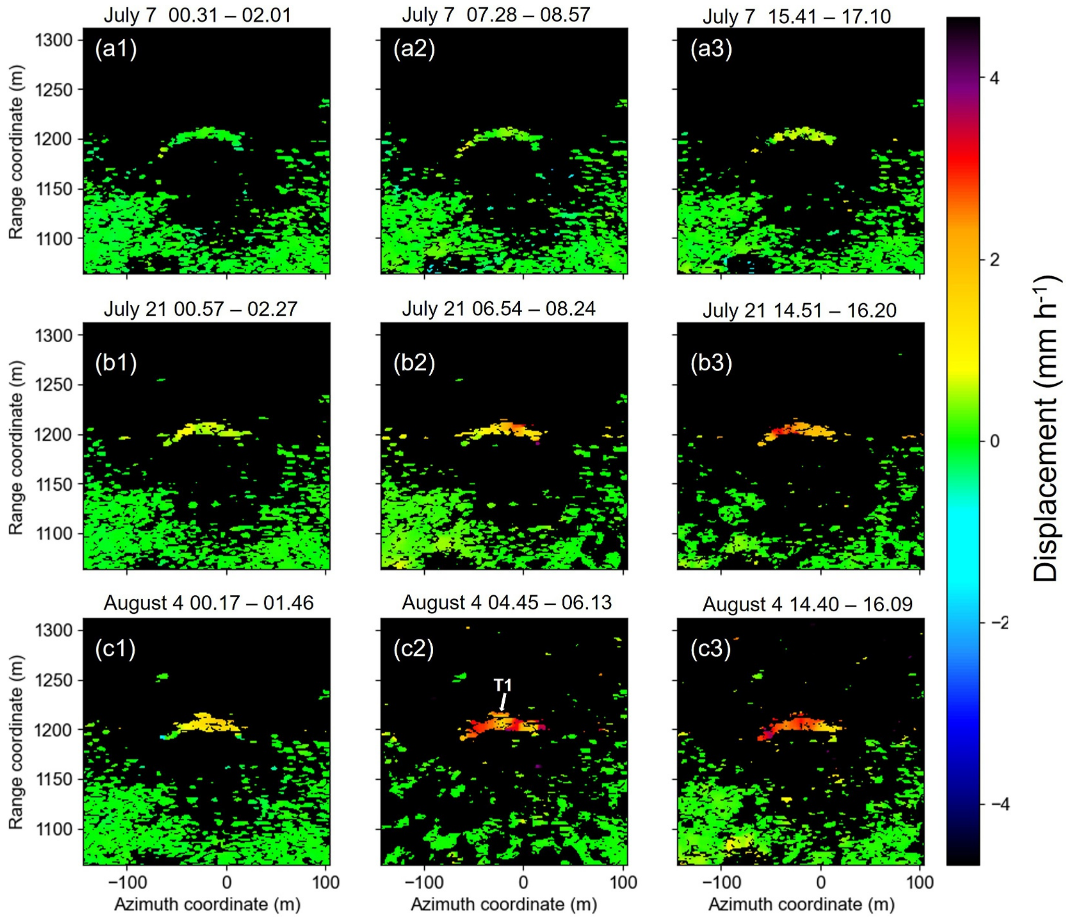

Figure 4. Different styles of diurnal variability from sample displacement maps of the ice cliff. Displacement maps are produced from stacked image pairs. (a1–a3): Diurnal variability observed on 7 July 2022 with little or no appreciable displacement in both night and day. (b1–b3): Diurnal variability observed on 21 July 2022 with displacement away from the line sight of the radar during the day and no displacement during the night. (c1–c3): Diurnal variability observed on August 4 with strong displacement away from the LOS of the radar at both day and night. In (c2) is marked the position of the transverse crevasse T1 which is referenced throughout the text. Positive values are displacement away from the radar, whereas negative values are displacement toward the radar system.

throughout the day with no apparent interruption (Figures 4c1–4c3) reaching ∼4 mm h^{-1}, amongst the maximum hourly displacement measured in the data set.

4.2. Measured Cumulative Displacement on the Ice Cliff: Observations of Spatial Variability

The cumulative sum of the displacements measured on the ice cliff is presented in Figure 5. The figure depicts results in 2D radar coordinates (Figure 5a), along-range profiles (Figure 5b) and point-cloud projected results (Figure 5c). Results reveal remarkable spatial variability. Displacement values reach ∼1,150 mm away from the sensor with peak values located in a well defined zone at the top of the ice cliff (zone A in Figure 5c). Total displacement on the foot of the ice cliff is almost three times lower and around 400 mm (zone B in Figure 5c). Another zone of relatively lower displacements is located on the western side of the ice cliff; this zone has been indicated with a white star and, as we will see in the next section, it is located in an area with appreciable ice-flow.

Along-range profiles highlight the presence of three different zones (Profiles 1 and 2 in Figure 5b). In the lowest-most portion (P1a and P2a in Figure 5b) ice cliff displacements are relatively uniform at around 400 mm away from the radar. The transition between the first and the second zone is marked by a change in the along-range gradient and the second layer exhibits a progressive increase in displacement with the range coordinate (P1b and P2b). The uppermost zone displays a reversal of the trend with decreasing along-range displacement. The

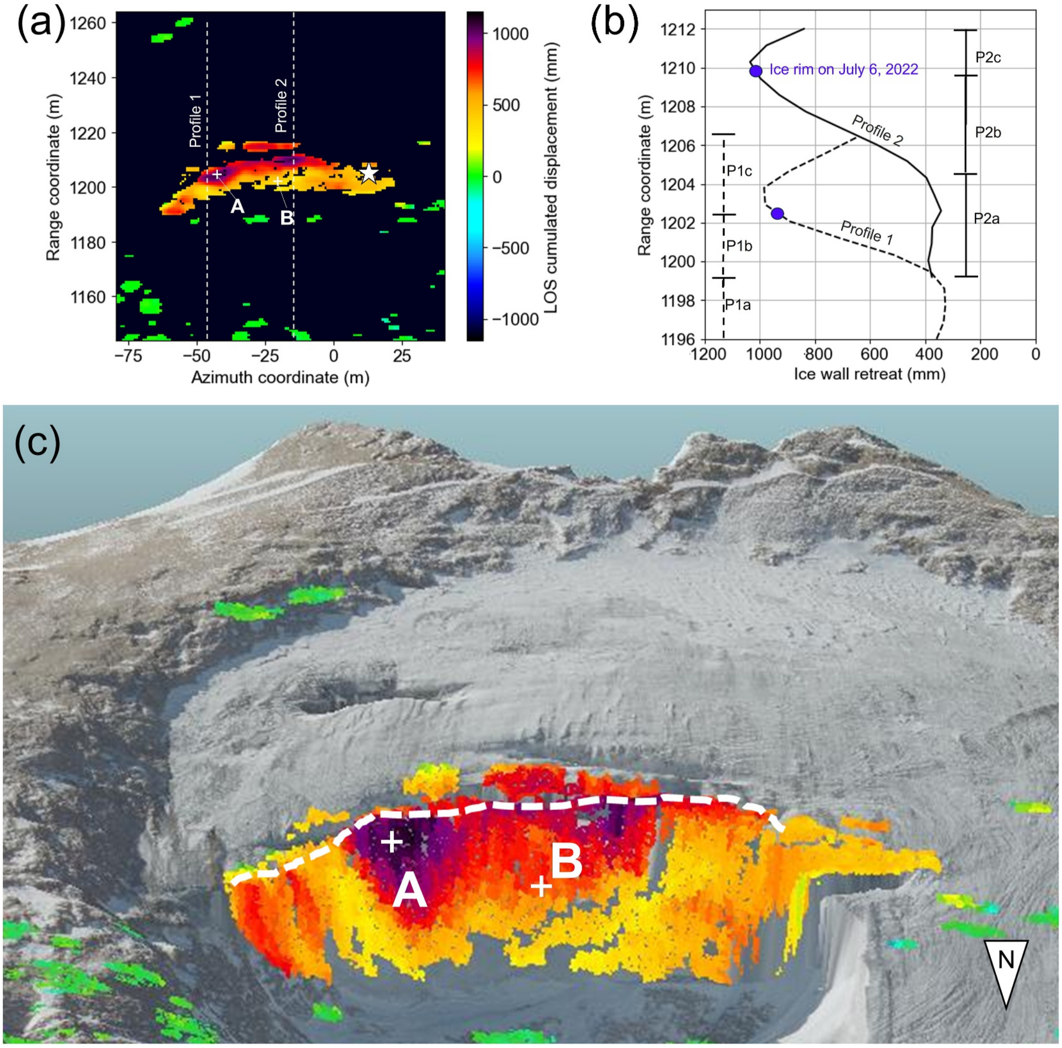

Figure 5. Spatial variability in the measured cumulative displacement measured along the LOS of the instrument on the ice cliff for the period 6 July–2 October 2022. (a) 2D map with positive displacement away from the sensor. The cross indicates the position of zone A whose temporal evolution is presented in Figure 6. The white star indicates the zone with relatively smaller displacement away from the LOS which corresponds to an area of faster ice motion toward the LOS. The two along-range profiles presented in (b) are also shown. (b) along-range ice-loss profiles extracted from (a). (c) results projected on a 3D point cloud of the glacier with indication of the ice cliff rim.

transition between the second and the third zone correspond with the ice-rim position at the beginning of the monitoring period.

4.3. Temporal Analysis of Measured Displacement: Daily and Sub-Daily Trends and Correlation With Air Temperature

The temporal evolution of measured cumulative displacement in both zone A (near the rim) and zone B (on the lower part of the cliff; see Figure 5) is strongly non-linear, with alternating periods of negligible displacement and intervals of significant movement away from the sensor (Figure 6a). Hourly displacement, smoothed using a 24-hr rolling mean, exhibits periodical fluctuations (Figure 6b). Smoothed hourly displacements at the rim reached the maximum value of 2.3 mm h^{-1} about twice those observed in zone B (1.1 mm h^{-1}). Displacement fluctuations generally follow the air temperature trends recorded at Punta Rocca.

We used the Spearman correlation coefficient (ρ) to evaluate the relationship between hourly displacement and air temperature (Figure 6c). Spearman's ρ was selected due to its robustness in identifying monotonic relationships

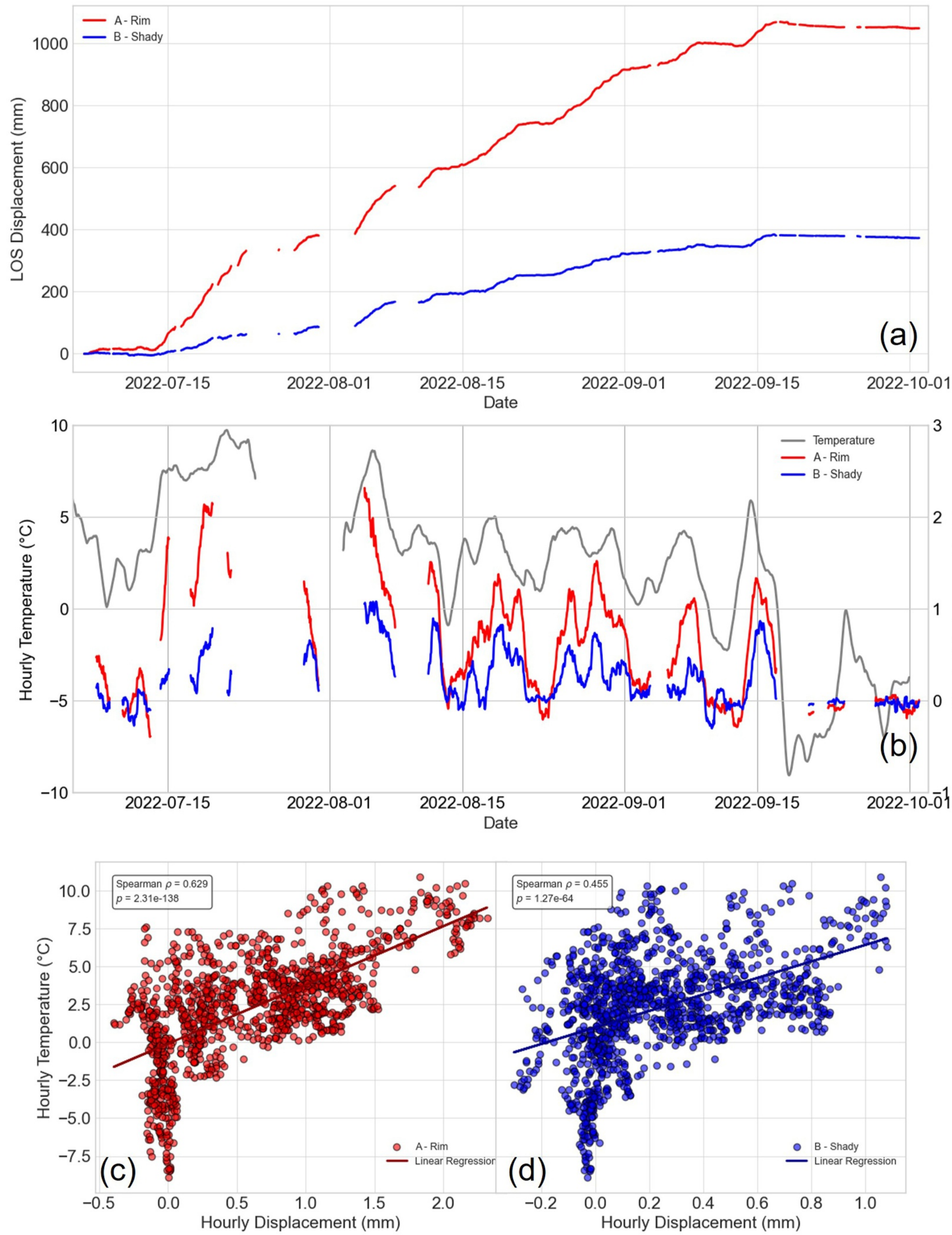

Figure 6. Temporal evolution of the measured cumulative displacement in zones A and B during the entire monitoring period. A and B positions are indicated in Figure 5. (a) Cumulative time-series; (b) hourly temperatures and hourly displacement smoothed using a 24 hr rolling window; (c) correlation between hourly temperature measured at Punta Rocca station and hourly displacement in zone A; (d) correlation between hourly temperature measured at Punta Rocca station and hourly displacement in zone B.

without assuming linearity or normality, which is appropriate for environmental data sets with potentially skewed distributions. For both zones, the p-values were extremely small, indicating statistically significant associations. ρ was higher for the rim (0.63) than for the shaded part of the cliff (0.46), suggesting a stronger monotonic relationship between displacement and temperature in zone A.

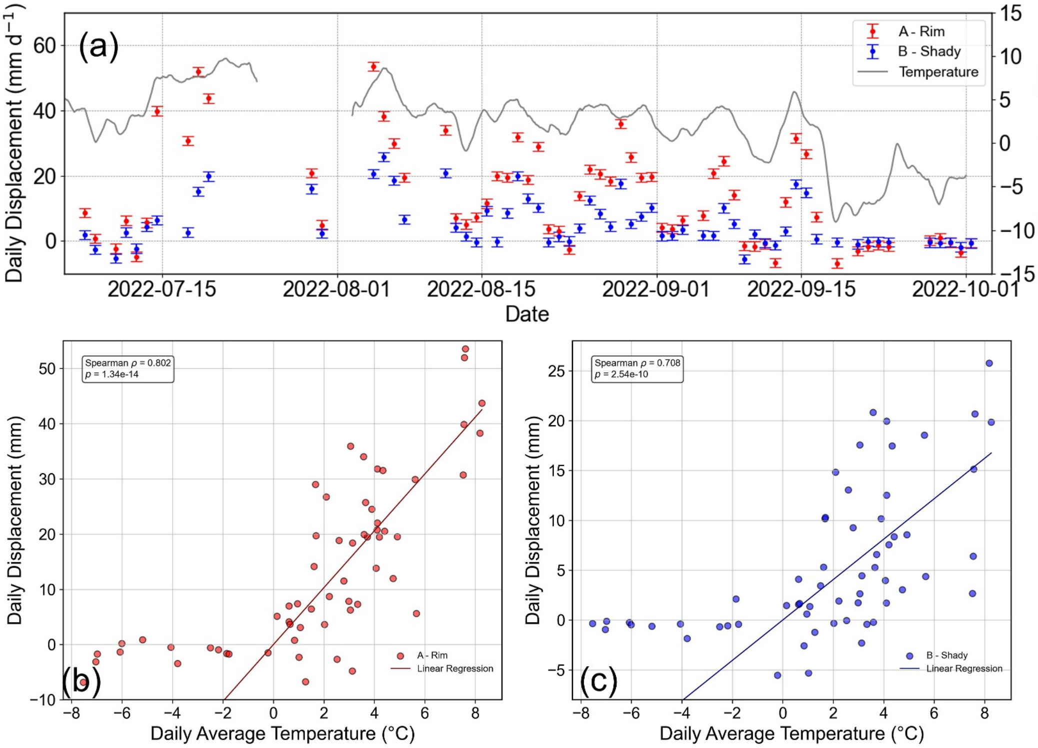

Figure 7. (a) Daily displacement in zones A and B during the 2022 ablation season. (b) Correlation between daily temperature measured at Punta Rocca station and daily displacement in zone A. (c) Correlation between daily temperature measured at Punta Rocca station and daily displacement in zone B.

Daily displacements also varied in tandem with air temperature (Figure 7a). On average, daily displacement in zone A was 2.3 times greater than in zone B. In zone A, on average daily displacement was negligible (-1.4 mm $\pm$ 1 mm d^{-1}) during the 13 days when the mean daily temperature (T) was below 0°C. Conversely, displacement rose markedly on warmer days, reaching up to 17.8 mm d^{-1} on days with $T > 0$°C, and up to 35 mm d^{-1} during the 7 warmest days with $T > 5$°C. The highest rate was observed on August 4, with 53 $\pm$ 1 mm d^{-1} in zone A at $T = 8$°C. Displacement ceased toward the end of the monitoring period as air temperatures dropped below freezing, marking the conclusion of the ablation season. The correlation between daily displacement and temperature remained statistically significant in both zones, with ρ values exceeding those observed in the hourly analysis (0.80 and 0.71 for A and B, respectively, Figure 7c).

4.4. Radar Images of the Ice Cliff

Examples of radar images from our data set are shown in Figure 8. The main feature of these images is the ice cliff, which appears as a bright series of radar reflections roughly aligned along the azimuth direction and forming a cord-shaped feature (Figure 8). The cliff is consistently visible in all radar images, although the patterns of the reflections did show some variations. While changes in reflectivity patterns are not the primary focus of this study, it is worth noting two main observations, which will be discussed later in the paper, as they relate to the evolution of the ice cliff during the season.

First, the extent of the cord-shaped brightly reflective area increased from ~800 m^2 on 6 July 2022 to ~1,400 m^2 on 2 October 2022. The values quoted here were derived by estimating the extent of the brightly reflective area from 2D images and therefore overestimate the real geometry because of the foreshortening effect which is typical of slopes inclined toward the radar (Wolff et al., 2024). Second, by comparing the four SAR images in Figure 8 we can observe the appearance of an upper reflector, starting from the second image of August 8. This upper reflector, which is visible only from August onwards, is indicated in Figure 8 with an arrow and is related to a transversal crevasse (T1) positioned above the main ice cliff (Figure 2).

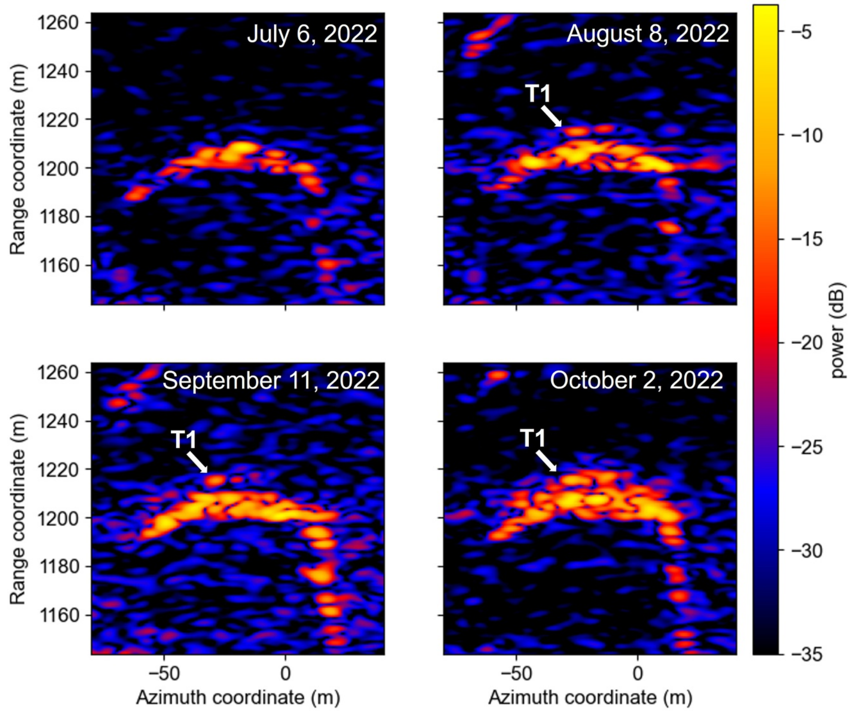

Figure 8. Examples of SAR images of the Marmolada Glacier ice cliff throughout the monitoring period. Radar amplitude is normalized with respect to their maximum and displayed with a dynamic range of 35 dB. The range and azimuth coordinates are measured in a Cartesian reference system having the middle point of the linear synthetic aperture as origin. The azimuth axis is along the rail and the range axis is perpendicular to it. The marking on the figure indicate the position of the transverse crevasse T1 which is referenced in the text.

4.5. Displacement Toward the LOS at the End of the Ablation Season

As noted previously, the average daily displacement in zone A during sub-freezing days was approximately -1.4 mm d^{-1}, indicating that small motion toward the sensor occurred under colder conditions. Beginning on September 17, mean daily air temperatures dropped below freezing, effectively halting melt and allowing for clearer interpretation of any LOS-directed motion. During this period (September 17–October 1), the net displacement measured at the cliff rim was predominantly oriented toward the LOS (negative values, Figure 9), with daily average rates approaching -2.5 mm d^{-1}. A distinct zone of enhanced motion, with average velocities between -5 and -7 mm d^{-1}, was evident in the western sector (white star in Figure 9).

4.6. Comparison Between Radar Data and Topographic Data

The comparison between ice-rim retreat estimates from 8 July to 20 September 2022 is shown in Figure 10. As mentioned in Section 3.5, TRI-derived displacements were corrected using a linear regression model between measured cumulative displacement and PDD. The regression gave an R^2 value of 0.99 and an RMSE of 14 mm, indicating an excellent fit and low residual variability (Figure 10). The p-value for the regression slope was $<10^{-44}$, confirming strong statistical significance. Based on this model, we estimated the correction factor Δ_{corr} to be 483 mm, and the total displacement T_{LOS} derived this way (TRI corrected in Figure 10) shows good agreement with the displacement obtained from differencing topographic data.

We acknowledge that more sophisticated gap-filling methods could be employed; however, pursuing such refinements is beyond the scope of this study and not essential to the main scientific objectives herein presented. The comparison (Figure 10) demonstrates that, even with this basic correction, TRI-based and topographic estimates of retreat are in agreement, supporting the reliability of both observational approaches.

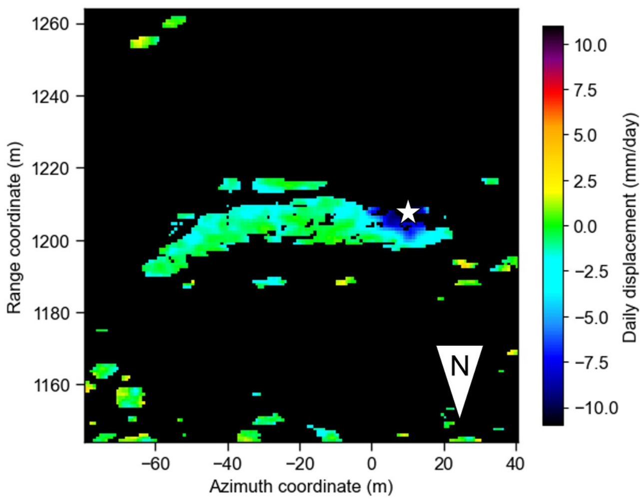

Figure 9. Evidence of residual ice flow during freezing conditions at the Marmolada glacier ice cliff. Average daily displacement map for the period 17 September to 1 October 2022. Negative displacement toward the LOS was ∼−2 ± 1 mm d^{-1} on the western part of the cliff and up to −6 ± 1 mm d^{-1} in the western part. The white star highlights the region with greater ice displacement.

5. Discussion

5.1. Evidence of Ice Dynamics Under Cold Conditions

Our monitoring approach allowed us to document the progressive backwasting of the Marmolada Glacier ice cliff in the period following the 2022 collapse. However, the measured net displacement recorded by TRI over this relatively slow moving ice body must comprise two principal contributions: (a) motion toward the sensor associated with internal ice deformation (negative measured displacement), and (b) retreat of the glacier away from the surface due to melt (positive measured displacement). While our measurements clearly indicate that ice loss was the dominant driver of measured LOS displacement during most of the ablation season, as the temperatures fell below freezing, we collected evidence for dynamical movement toward the sensor. Although the primary focus of this study is the post-collapse retreat, the observed spatial variability reported in Figure 9 point to the complexity of glacier flow on this relatively small glacier.

Recent investigations at the Marmolada have demonstrated that, at the time of failure, the glacier was likely cold based (Francese et al., 2024), implying negligible basal sliding. Under such conditions, ice deformation primarily occurs through internal creep, resulting in vertical velocity profiles characterized by higher speeds near the surface than at the base. This theoretical pattern is broadly consistent with our results from the late part of the monitoring (Figure 9) with displacement toward the LOS higher in the uppermost part of the cliff. Moreover, the presence of a region with relatively faster motion to the west agrees with the recent findings by Francese et al. (2024), who showed that ice thickness in the western part of the cliff is greater, locally promoting higher velocities there.

While a more robust assessment of spatial variations in ice flow would require the integration of TRI observations with glacier flow modeling, this analysis lies beyond the scope of the present study. Nevertheless, our results suggest that even in a slow moving ice body such as the remaining Marmolada ice cliff, there is a systematic

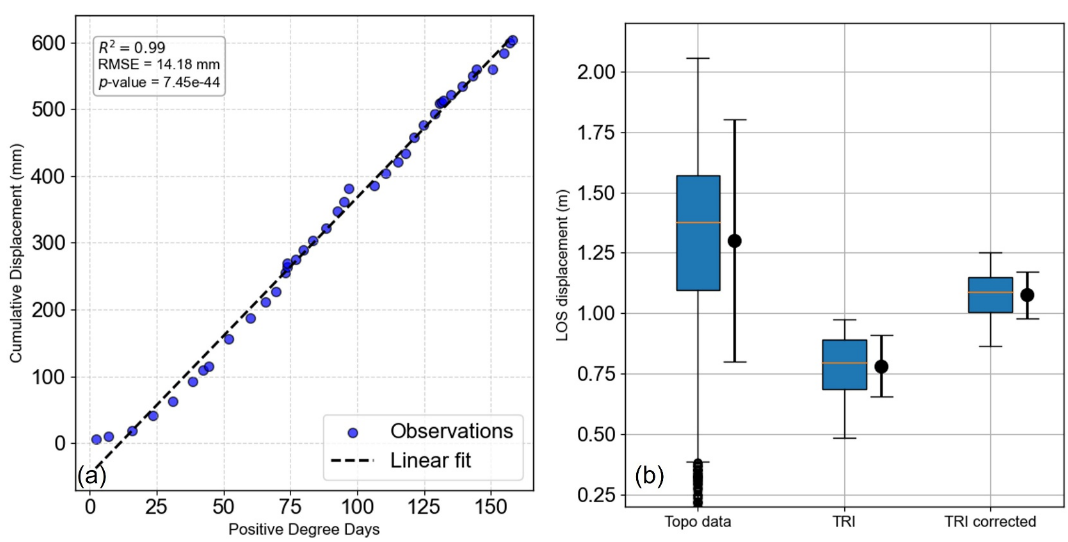

Figure 10. (a) Linear regression model between positive degree days and measured cumulative displacement on the ice cliff rim. (b) Estimates of ice cliff retreat measured along the LOS from topographic data (TOPO DATA), partial radar cumulative displacement uncorrected for missing data (TRI), total cumulative displacement derived from the linear relationship between Positive Degree Day and measured cumulative displacement (TRI corrected). All estimates refer to the cliff's rim on the period between 8 July and 20 September 2022. Results are given in two ways: (i) boxplots with median value and (ii) mean value ± one standard deviation from the mean.

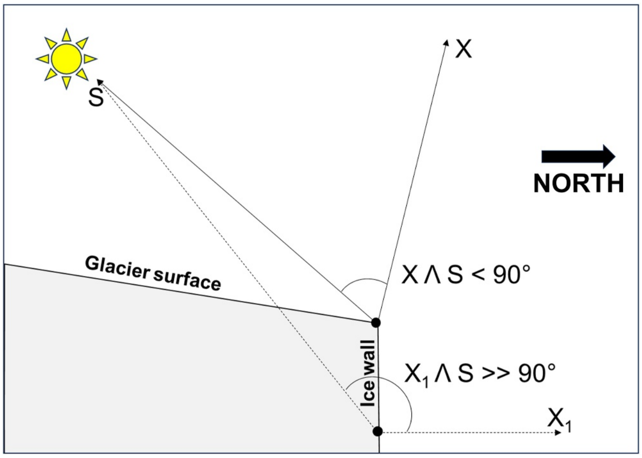

Figure 11. Conceptual model of the post-collapse configuration of the Marmolada ice cliff with reference vectors used in Equation 1.

underestimation of radar-derived ice melt due to unaccounted ice flow. For most of the ice cliff, this effect is minor. However, in the western section, the discrepancy becomes more pronounced, with measured TRI displacement values approximately 500–600 mm lower than in the western sector (Figure 5, white star). A sustained LOS-directed motion of -6 mm d^{-1} for the entire 91 days of monitoring would account for an additional 550 mm of displacement, consistent with the observed differences.

5.2. Post-Collapse Backwasting at the Marmolada Ice Cliff

The results presented here provide new indications about how the Marmolada ice cliff backwasted throughout the melt season. During the monitoring period, we did not detect any new collapses or calving, so the retreat was primarily driven by melt. We also observed that measured melt at the very top of the cliff is about three times higher than on the main vertical wall (Figure 5). Furthermore, along-range profiles (Figure 5b) suggest that melt on the steep wall was fairly uniform, while it increased upward toward the rim, reaching a maximum at the rim position at the start of the monitoring period. This indicates that the greatest ice loss occurred at the rim, raising the question of what processes are responsible for this pattern.

Following the collapse, the shape of the ice cliff was fairly simple with an idealized cross section in which a gently sloping ice surface ended into a vertical cliff (Figure 11). This geometry leads to two entirely different configurations in terms of received solar radiation as the ice on the gentle slope could receive direct sunlight whereas on the vertical wall it was mainly in the shade. To quantify this effect, we can calculate the incoming shortwave solar radiation on a sloped surface as follows (Garnier & Ohmura, 1968):

$$I_d = I_0 \cos(X \wedge S), \tag{1}$$

where I_d is the solar radiation on a given slope for a sloped unit area, I_0 is the observed solar radiation at a horizontal plane, X is a unit coordinate vector normal to the slope and pointing away from the ground, S is a unit coordinate vector expressing the height and the position of the sun and $\wedge$ is a symbol indicating the angle between X and S. As shown by Equation 1, the angle between the surface normal and the sun, $X \wedge S$, is obtuse for the vertical wall, so the wall stays in the shade, while on the upper slope the angle is acute and this allows direct sunlight. A numerical example from Garnier and Ohmura (1968) illustrates this: at 45°N during the Autumnal Equinox, a 30° slope receives 135.2 ly day^{-1} whereas slopes steeper than 50° are completely shaded.

Stronger melt at the rim gradually flattened the upper part of the cliff, while the vertical face remained steep because it was protected by direct solar radiation. The slightly lower correlation between measured displacement and air temperature in the shaded zones (Figures 6 and 7) also supports this interpretation. The Punta Rocca station is in full sun and therefore its air temperature relates better to the rim region than to the shaded parts. The higher Spearman correlation at the rim (daily value $\rho = 0.8$) is similar to the value of 0.89 found at Belvedere Glacier by Ioli et al. (2024), while the somewhat lower value in the shaded part ($\rho = 0.7$) indicates that small-scale microclimate differences are important and should be further investigated, for example, with detailed energy-balance modeling (e.g., Buri et al. (2021)).

Another interesting aspect is the apparent decrease of cumulative displacement beyond the initial rim position (P1c and P2c in Figure 5b). It is important to clarify that this is very likely not a physical signal of reduced melt, but an effect related to the radar technique. As shown in Figure 12a, when the cliff retreats from R_1 to R_2 and later to R_3, the surface areas located at $R > R_1$ enter the radar LOS only later in time. Therefore, they show smaller cumulative displacement simply because the radar observed them for a shorter period.

These findings are also supported by radar intensity data. The along-range extension of the radar return increased over time, and the reflection from crevasse T1 became visible only during the second part of the monitoring (Figure 8). This suggests that melt gradually removed material from the upper part of the cliff, exposing ice that

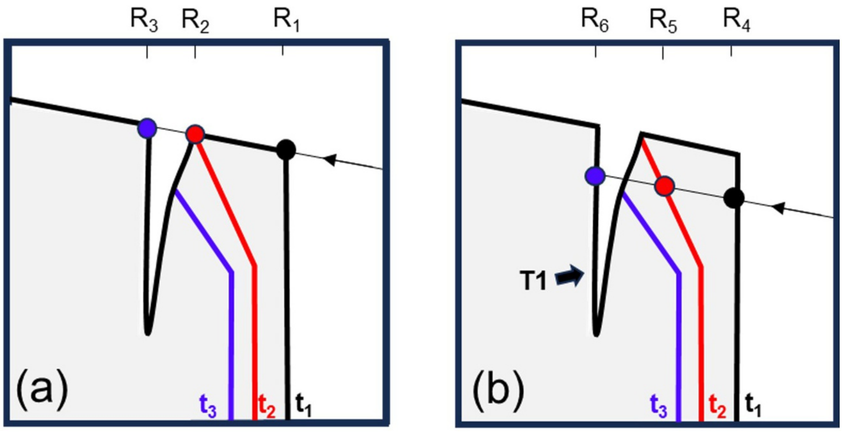

Figure 12. Conceptual models of ice cliff evolution and surface interaction with idealized radar-beams approximated by linear vectors. (a) Explanation of the apparent inversion in displacement trend for range position (R) higher than R_1. The range coordinate of the ice cliff rim changes from $R_1 < R_2 < R_3$ as the time increases from t_1 to t_3; this phenomenon causes both an increase of the reflector's length in the along-range direction and peak measured cumulative displacement at R_1.
(b) Explanation for the appearance of the crevasse T1 at a later stage in the monitoring: the transverse crevasse T1 at range coordinate R_6 remains out of the radar-sight until t_3.

was hidden at the beginning. This behavior is sketched in Figure 12b, where the reflecting surface shifts from R_4 to R_5, and later to R_6 when the crevasse comes into the radar view.

These considerations show that TRI measurements offer very useful information for studying the evolution of ice cliffs, but they also require careful interpretation. Because the ice surface changes quickly, the LOS of the radar strongly controls which areas are visible at any moment. A simple, direct reading of Figure 5 could incorrectly suggest that ice loss at crevasse T1 is smaller than at the rim, while in reality T1 was under radar sight for less time. For this reason, TRI derived spatial patterns should always be analyzed together with the evolving geometry of the surface.

5.3. Implications and Future Work

The first implication of the results presented in our study is that the mass loss of slowly moving ice cliffs can be monitored in near real-time using TRI. To the best of our knowledge, this is the first time that such an application is documented in the literature. Near-continuous measurements of ice melt on glaciers are generally quite difficult as it involves direct in situ operations and the deployment of personnel at high altitude (Carturan et al., 2019; Len Keeler & Brugger, 2012; Netto & Arigony-Neto, 2019). TRI, deployed in proximity of mountain huts or similar strategic locations, may prove to be a valuable tool in developing glaciological now-casting programs to assess, in-real time, the state of glaciers and high-altitude ice masses. The effort of developing sustainable and reliable glacier monitoring procedures appears to be very relevant, particularly in the European Alps, where thousands of mountaineers access glacierized peaks all year round.

It is important to highlight the fact that the Marmolada ice cliff represented an optimal target to study the application of TRI for ice melt detection. The July 3 avalanche left a sub-vertical wall of slowly moving ice and indeed, during the entire monitoring period, the main component of displacement was not toward the sensor, at least on the main body of the ice cliff. On larger, faster ice bodies the net detectable displacement is typically toward the sensor (Liu et al., 2019) and therefore, on such conditions, it is impossible to obtain ice loss estimates. However, with TRI it is possible to monitor multiple targets within the same mountain slope and, for example, a potential scenario for future applications could be the joint monitoring of ice melt on slowly moving ice cliffs or ice aprons (Ravanel et al., 2023), as well as the flow of avalanching glaciers. A combination of multiple techniques (e.g., GNSS, satellite feature tracking or reflective prisms), combined with the TRI method, could also provide the opportunity to evaluate both the flow regime and the ice melt of glaciers.

The capability of detailing ice ablation processes on ice cliffs may unlock the potential for future research on steep ice and ice cliff melting patterns. Ice cliff melt dynamics are still a subject of active research as they are thought to be an important, yet poorly understood, contributor for the water balance of debris-covered glaciers (Buri et al., 2021;

Steiner et al., 2019). These cliffs vary in size, but they can reach more than 100 m in width and 30 m in height (Steiner et al., 2019); from a metrological point of view, these geometries represent an optimal target for TRI.

6. Conclusions

In this study we used terrestrial radar interferometry (TRI) to investigate the post-collapse evolution of the Marmolada Glacier ice cliff following its catastrophic collapse on 3 July 2022. As a part of the national emergency response that followed the event, we deployed a radar interferometer 1.2 km north of the ice cliff and initiated a near-continuous monitoring effort that lasted throughout the entire ablation season. The newly exposed, sub-vertical ice cliff represented an optimal target for the TRI technique. Contrary to expectations based on other events documented in the literature, no evidence of significant downslope motion or secondary collapses was detected. Instead, our measurements revealed progressive ice cliff backwasting driven by surface melt, with measured cumulative displacements of up to 1.2 m away from the sensor at the sun-exposed cliff rim and about three times lower on the lower, shadier foot. The spatial pattern of ice loss on the ice cliff suggested the presence of two different melt zones with a basal portion experiencing a small but uniform melt and a topmost zone with increasing melt with height. The observed spatial variability is consistent with the commonly observed ice cliff morphology with a steep ice face capped by a flatter, gently sloping edge, and such a morphology is the result of higher solar radiation at the top compared to the wall. Radar estimates of ice cliff retreat agree with independent estimates from topographic surveys.

Daily backwasting rates peaked at 53 ± 1 mm d^{-1}, but when air temperatures dropped below freezing, the ice cliff no longer retreated and instead exhibited small displacements toward the radar (up to—6 mm d^{-1}), consistent with downslope ice flow in the absence of melt. These findings suggest that TRI can be used to monitor detailed dynamics of steep ice cliffs. However, they also demonstrate the complexity of TRI in glacier monitoring as observed displacements reflect the combined effects of ice flow toward the sensor and ice melt away from the sensor. Future efforts should integrate TRI measurements, energy balance modeling, direct radiation measurements, and glacier flow simulations to study the processes involved, improve hazard assessment, and ultimately improve our understanding of the complex behavior of unstable ice masses in a warming climate.

Conflict of Interest

The authors declare no conflicts of interest relevant to this study.

Data Availability Statement

Displacement maps, topographic data, air temperature data, and displacement time-series that support the findings described in this study can be found in Gusmeroli (2025).

Acknowledgments
This work was financially supported by the Italian Department of Civil Protection (Dipartimento della Protezione Civile—Presidenza del Consiglio dei Ministri) and by the Province of Trento (Provincia autonoma di Trento). The Province of Trento also provided essential logistic support to the monitoring campaign and acquired the high-resolution topographic data set of the area of interest in September 2022. Arrigo Avi and the fire brigade of the Province of Trento are acknowledged for acquiring the high-resolution topographic data set of the area of interest in July 2022. The editor Ann Rowan, Fabrizio Troilo and two anonymous reviewers provided thoughtful comments that substantially improved the manuscript. We finally thank Alessandro Castiglione, Massimiliano Nocentini, Giovanni Gigli, and Luca Lombardi for their help in the field deployment of the instrumentation. Open access publishing facilitated by Università degli Studi di Firenze, as part of the Wiley - CRUI-CARE agreement.

References

Alean, J. (1985). Ice avalanches: Some empirical information about their formation and reach. *Journal of Glaciology*, *31*(109), 324–333. https://doi.org/10.3189/S0022143000006663

Allstadt, K. E., Shean, D. E., Campbell, A., Fahnestock, M., & Malone, S. D. (2015). Observations of seasonal and diurnal glacier velocities at Mount Rainier, Washington, using terrestrial radar interferometry. *The Cryosphere*, *9*(6), 2219–2235. https://doi.org/10.5194/tc-9-2219-2015

Bondesan, A., & Francese, R. G. (2023). The climate-driven disaster of the Marmolada Glacier (Italy). *Geomorphology*, *431*, 108687. https://doi.org/10.1016/j.geomorph.2023.108687

Braithwaite, R. J. (1995). Positive degree-day factors for ablation on the Greenland ice sheet studied by energy-balance modelling. *Journal of Glaciology*, *41*(137), 153–160. https://doi.org/10.3189/S0022143000017846

Buri, P., Miles, E. S., Steiner, J. F., Ragettli, S., & Pellicciotti, F. (2021). Supraglacial ice cliffs can substantially increase the mass loss of debris-covered glaciers. *Geophysical Research Letters*, *48*(6), e2020GL092150. https://doi.org/10.1029/2020GL092150

Carlà, T., Gigli, G., Lombardi, L., Nocentini, M., Gracchi, T., Rossi, G., et al. (2024). Mechanisms of block instability at the toe of a slowly deforming rock slope. *Rock Mechanics and Rock Engineering*, *57*(3), 1543–1563. https://doi.org/10.1007/s00603-023-03674-9

Carlà, T., Nolesini, T., Solari, L., Rivolta, C., Dei Cas, L., & Casagli, N. (2019). Rockfall forecasting and risk management along a major transportation corridor in the Alps through ground-based radar interferometry. *Landslides*, *16*(8), 1425–1435. https://doi.org/10.1007/s10346-019-01190-y

Carturan, L., CazorzìI, F., Dalla Fontana, G., & Zanoner, T. (2019). Automatic measurement of glacier ice ablation using thermistor strings. *Journal of Glaciology*, *65*(250), 188–194. https://doi.org/10.1017/jog.2018.103

Casagli, N., Intrieri, E., Tofani, V., Gigli, G., & Raspini, F. (2023). Landslide detection, monitoring and prediction with remote-sensing techniques. *Nature Reviews Earth & Environment*, *4*(1), 51–64. https://doi.org/10.1038/s43017-022-00373-x

Chiarle, M., Viani, C., Mortara, G., Deline, P., Tamburini, A., & Nigrelli, G. (2022). Large glacier failures in the Italian Alps over the last 90 years. *Geografia Fisica e Dinamica Quaternaria*, *45*(1), 19–40. https://doi.org/10.4461/GFDQ.2022.45.2

Chmiel, M., Walter, F., Pralong, A., Preiswerk, L., Funk, M., Meier, L., & Brenguier, F. (2023). Seismic constraints on damage growth within an unstable hanging glacier. *Geophysical Research Letters*, *50*(9), e2022GL102007. https://doi.org/10.1029/2022GL102007

Cooper, M. G., & Smith, L. C. (2019). Satellite remote sensing of the Greenland ice sheet ablation zone: A review. *Remote Sensing*, *11*(20), 2405. https://doi.org/10.3390/rs11202405

Crosta, G. B., di Prisco, C., Frattini, P., Frigerio, G., Castellanza, R., & Agliardi, F. (2014). Chasing a complete understanding of the triggering mechanisms of a large rapidly evolving rockslide. *Landslides*, *11*(5), 747–764. https://doi.org/10.1007/s10346-013-0433-1

Di Traglia, F., Nolesini, T., Intrieri, E., Mugnai, F., Leva, D., Rosi, M., & Casagli, N. (2014). Review of ten years of volcano deformations recorded by the ground-based InSAR monitoring system at Stromboli volcano: A tool to mitigate volcano flank dynamics and intense volcanic activity. *Earth-Science Reviews*, *139*, 317–335. https://doi.org/10.1016/j.earscirev.2014.09.011

Faillettaz, J., Funk, M., & Sornette, D. (2011). Icequakes coupled with surface displacements for predicting glacier break-off. *Journal of Glaciology*, *57*(203), 453–460. https://doi.org/10.3189/002214311796905668

Faillettaz, J., Funk, M., & Vagliasindi, M. (2016). Time forecast of a break-off event from a hanging glacier. *The Cryosphere*, *10*(3), 1191–1200. https://doi.org/10.5194/tc-10-1191-2016

Faillettaz, J., Funk, M., & Vincent, C. (2015). Avalanching glacier instabilities: Review on processes and early warning perspectives. *Reviews of Geophysics*, *53*(2), 203–224. https://doi.org/10.1002/2014RG000466

Fortuny, J., & Sieber, A. (1994). Fast algorithm for a near-field synthetic aperture radar processor. *IEEE Transactions on Antennas and Propagation*, *42*(10), 1458–1460. https://doi.org/10.1109/8.320756

Francese, R. G., Valentino, R., Haeberli, W., Bondesan, A., Giorgi, M., Picotti, S., et al. (2024). Failure of Marmolada Glacier (Dolomites, Italy) in 2022: Data-based back analysis of possible collapse mechanisms as related to recent morpho-climatic evolution and possible trigger factors. *Natural Hazards and Earth System Sciences Discussions*, *2024*, 1–41. https://doi.org/10.5194/nhess-2024-212

Garnier, B., & Ohmura, A. (1968). A method of calculating the direct shortwave radiation income of slopes. *Journal of Applied Meteorology*, *7*(5), 796–800. https://doi.org/10.1175/1520-0450(1968)007<0796:amoctd>2.0.co;2

Giordan, D., Dematteis, N., Allasia, P., & Motta, E. (2020). Classification and kinematics of the planpincieux glacier break-offs using photographic time-lapse analysis. *Journal of Glaciology*, *66*(256), 188–202. https://doi.org/10.1017/jog.2019.99

Goldstein, R., Zebker, H., & Werner, C. (1988). Satellite radar interferometry: Two-dimensional phase unwrapping. *Radio Science*, *23*(4), 713–720. https://doi.org/10.1029/RS023i004p00713

Gusmeroli, A. (2025). Data from Post-collapse ice cliff backwasting at the Marmolada Glacier observed by terrestrial radar interferometry [Dataset]. https://doi.org/10.5281/zenodo.16759274

Hock, R. (1999). A distributed temperature-index ice- and snowmelt model including potential direct solar radiation. *Journal of Glaciology*, *45*(149), 101–111. https://doi.org/10.3189/S0022143000003087

Iken, A. (1977). Movement of a large ice mass before breaking off. *Journal of Glaciology*, *19*(81), 595–605. https://doi.org/10.3189/S0022143000215505

Ioli, F., Dematteis, N., Giordan, D., Nex, F., & Pinto, L. (2024). Deep learning low-cost photogrammetry for 4D short-term Glacier dynamics monitoring. *PFG—Journal of Photogrammetry, Remote Sensing and Geoinformation Science*, *92*(6), 657–678. https://doi.org/10.1007/s41064-023-00272-w

Jacquemart, M., Weber, S., Chiarle, M., Chmiel, M., Cicoira, A., Corona, C., et al. (2024). Detecting the impact of climate change on alpine mass movements in observational records from the European Alps. *Earth-Science Reviews*, *258*, 104886. https://doi.org/10.1016/j.earscirev.2024.104886

Kristensen, L., Czekirda, J., Penna, I., Etzelmüller, B., Nicolet, P., Pullarello, J. S., et al. (2021). Movements, failure and climatic control of the Veslemannen rockslide, Western Norway. *Landslides*, *18*(6), 1963–1980. https://doi.org/10.1007/s10346-020-01609-x

Len Keeler, M., & Brugger, K. A. (2012). A method for recording ice ablation using a low-cost ultrasonic rangefinder. *Journal of Glaciology*, *58*(209), 565–568. https://doi.org/10.3189/2012JoG11J153

Leva, D., Nico, G., Tarchi, D., Fortuny-Guasch, J., & Sieber, A. (2003). Temporal analysis of a landslide by means of a ground-based SAR interferometer. *IEEE Transactions on Geoscience and Remote Sensing*, *41*(4), 745–752. https://doi.org/10.1109/TGRS.2003.808902

Liu, L., Jiang, L., Sun, Y., Wang, H., Sun, Y., & Xu, H. (2019). Diurnal fluctuations of glacier surface velocity observed with terrestrial radar interferometry at Laohugou No. 12 Glacier, western Qilian Mountains, China. *Journal of Glaciology*, *65*(250), 239–248. https://doi.org/10.1017/jog.2019.1

Lombardi, L., Nocentini, M., Frodella, W., Nolesini, T., Bardi, F., Intrieri, E., et al. (2017). The Calatabiano landslide (southern Italy): Preliminary GB-InSAR monitoring data and remote 3D mapping. *Landslides*, *14*(2), 685–696. https://doi.org/10.1007/s10346-016-0767-6

Margreth, S., Funk, M., Tobler, D., Dalban, P., Meier, L., & Lauper, J. (2017). Analysis of the hazard caused by ice avalanches from the hanging Glaier on the Eiger west face. *Cold Regions Science and Technology*, *144*, 63–72. (International Snow Science Workshop 2016 Breckenridge). https://doi.org/10.1016/j.coldregions.2017.05.012

Netto, G. T., & Arigony-Neto, J. (2019). Open-source automatic weather station and electronic ablation station for measuring the impacts of climate change on glaciers. *HardwareX*, *5*, e00053. https://doi.org/10.1016/j.ohx.2019.e00053

Noferini, L., Mecatti, D., Macaluso, G., Pieraccini, M., & Atzeni, C. (2009). Monitoring of Belvedere Glacier using a wide angle GB-SAR interferometer. *Journal of Applied Geophysics*, *68*(2), 289–293. https://doi.org/10.1016/j.jappgeo.2009.02.004

Ohmura, A. (2001). Physical basis for the temperature-based melt-index method. *Journal of Applied Meteorology and Climatology*, *40*(4), 753–761. https://doi.org/10.1175/1520-0450(2001)040⟨0753:PBFTTB⟩2.0.CO;2

Paul, F., Rastner, P., Azzoni, R. S., Diolaiuti, G., Fugazza, D., Le Bris, R., et al. (2019). Glacier inventory of the Alps from Sentinel-2, shape files [Dataset]. *PANGAEA*. https://doi.org/10.1594/PANGAEA.909133

Perret, P., Fosson, J. P., Mondardini, L., & Segor, V. (2021). Val Ferret Pilot Action Region: Grandes Jorasses Glaciers—An open-air laboratory for the development of close-range remote sensing monitoring systems. In J. Beguš, F. Berger, & K. Kleemayr (Eds.), *Best practice examples of implementing ecosystem-based natural hazard risk management in the GreenRisk4ALPs Pilot Action Regions (chap. 3)*. Rijeka: IntechOpen. https://doi.org/10.5772/intechopen.99013

Pieraccini, M., & Miccinesi, L. (2019). Ground-based radar interferometry: A bibliographic review. *Remote Sensing*, *11*(9), 1029. https://doi.org/10.3390/rs11091029

Pralong, A., & Funk, M. (2006). On the instability of avalanching glaciers. *Journal of Glaciology*, *52*(176), 31–48. https://doi.org/10.3189/172756506781828980

Ravanel, L., Guillet, G., Kaushik, S., Preunkert, S., Malet, E., Magnin, F., et al. (2023). Ice aprons on steep high-alpine slopes: Insights from the Mont-Blanc massif, Western Alps. *Journal of Glaciology*, *69*(277), 1275–1291. https://doi.org/10.1017/jog.2023.15

Riesen, P., Strozzi, T., Bauder, A., Wiesmann, A., & Funk, M. (2011). Short-term surface ice motion variations measured with a ground-based portable real aperture radar interferometer. *Journal of Glaciology*, *57*(201), 53–60. https://doi.org/10.3189/002214311795306718

Röthlisberger, H. (1977). Ice avalanches. *Journal of Glaciology*, *19*(81), 669–671. https://doi.org/10.3189/S0022143000029580
Rott, H., & Mätzler, C. (1987). Possibilities and limits of synthetic aperture radar for snow and glacier surveying. *Annals of Glaciology*, *9*, 195–199. https://doi.org/10.3189/S0260305500000604
Rouyet, L., Kristensen, L., Derron, M.-H., Michoud, C., Blikra, L. H., Jaboyedoff, M., & Lauknes, T. R. (2017). Evidence of rock slope breathing using ground-based InSAR. *Geomorphology*, *289*, 152–169. https://doi.org/10.1016/j.geomorph.2016.07.005
Skrede, I., Kristensen, L., & Rivolta, C. (2016). Use of ground based INSAR Radar to monitor glide avalanches. In *Proceedings, International Snow Science Workshop, Breckenridge, Colorado* (pp. 51–57).
Steiner, J. F., Buri, P., Miles, E. S., Ragettli, S., & Pellicciotti, F. (2019). Supraglacial ice cliffs and ponds on debris-covered glaciers: Spatio-temporal distribution and characteristics. *Journal of Glaciology*, *65*(252), 617–632. https://doi.org/10.1017/jog.2019.40
Tarchi, D., Casagli, N., Moretti, S., Leva, D., & Sieber, A. J. (2003). Monitoring landslide displacements by using ground-based synthetic aperture radar interferometry: Application to the Ruinon landslide in the Italian Alps. *Journal of Geophysical Research*, *108*(B8). https://doi.org/10.1029/2002JB002204
Tarchi, D., Rudolf, H., Luzi, G., Chiarantini, L., Coppo, P., & Sieber, A. (1999). SAR interferometry for structural changes detection: A demonstration test on a dam. In *International Geoscience and Remote Sensing Symposium* (Vol. 3, pp. 1522–1524). https://doi.org/10.1109/IGARSS.1999.772006
Tarquini, S., Isola, I., Favalli, M., Mazzarini, F., Bisson, M., Pareschi, M. T., & Boschi, E. (2007). TINITALY/01: A new Triangular Irregular Network of Italy. *Annals of Geophysics*, *50*(3), 407–425. https://doi.org/10.4401/ag-442
Topping, J. (1972). *Errors observation and their treatment*. Chapman and Hall.
Wolff, C., Derron, M.-H., Rivolta, C., & Jaboyedoff, M. (2024). A tool for estimating ground-based InSAR acquisition characteristics prior to monitoring installation and survey and its differences from satellite InSAR. *Geoscientific Instrumentation, Methods and Data Systems*, *13*(2), 225–248. https://doi.org/10.5194/gi-13-225-2024